Supplementary Information for Coherent control of an ultrabright single spin in hexagonal boron nitride at room temperature

Nai-Jie Guo,[1,2,3,*] Song Li,[4,*] Yuan-Ze Yang,[1,2,3,*] Xiao-Dong Zeng,[1,2,3,*] Shang Yu,[1,2,3] Yu Meng,[1,2,3] Zhi-Peng Li,[1,2,3] Zhao-An Wang,[1,2,3] Lin-Ke Xie,[1,2,3] Rong-Chun Ge,[5] Jun-Feng Wang,[1,2,3,5] Qiang Li,[1,2,3] Jin-Shi Xu,[1,2,3] Wei Liu,[1,2,3,†] Yi-Tao Wang,[1,2,3,‡] Jian-Shun Tang,[1,2,3,§] Adam Gali,[4,6,¶] Chuan-Feng Li,[1,2,3,**] and Guang-Can Guo[1,2,3]

[1] *CAS Key Laboratory of Quantum Information, University of Science and Technology of China, Hefei, Anhui 230026, China.*
[2] *CAS Center For Excellence in Quantum Information and Quantum Physics, University of Science and Technology of China, Hefei, Anhui 230026, China.*
[3] *Hefei National Laboratory, University of Science and Technology of China, Hefei 230088, China*
[4] *Wigner Research Centre for Physics, H-1121 Budapest, Hungary*
[5] *College of Physics, Sichuan University, Chengdu China, 610064*
[6] *Department of Atomic Physics, Institute of Physics, Budapest University of Technology and Economics, H-1111 Budapest, Hungary*

I. SUPPLEMENTARY NOTE 1

The correction of emission rate of Defect A. The saturated emission rate $I_{\rm sat}$ measured in the experiment is $\sim 3.7 \times 10^6$ counts/s. The corrected emission rate $I_{\rm sat}^{\rm corrected}$ can be written as $I_{sat}^{corrected} = I_{sat}/\eta$, where η is the loss coefficient. The loss coefficient η is $\sim 14.9\%$ (including objective collection efficiency considering the reflection of the gold film (56%), fiber coupling efficiency (38%), and detection efficiency of single photon detector (70%)). Therefore, we can calculate that $I_{sat}^{corrected} = 2.5 \times 10^7$ counts/s.

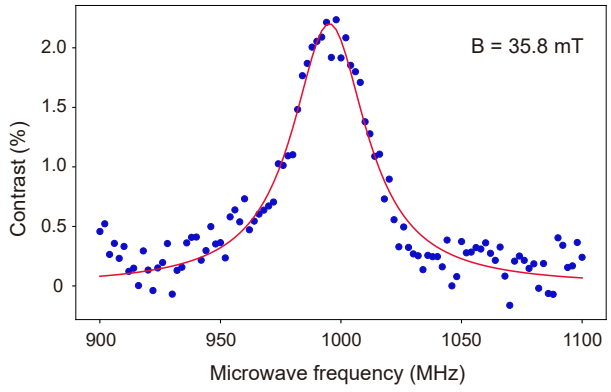

FIG. S1: **ODMR spectrum of Defect A.** The room-temperature ODMR spectrum of Defect A at 35.8-mT external magnetic field exhibits a positive peak at 970 MHz, whose contrast exceeds 2% and FWHM is $\sim$ 37 MHz.

II. SUPPLEMENTARY NOTE 2

A relatively higher ODMR contrast. Fig. S1 shows a room-temperature ODMR spectrum with a contrast of more than 2% for Defect A. This value was obtained when the sample was first tested, and the difference may be induced by the variations of experimental conditions, especially the resistance that affects the microwave radiation efficiency. Nevertheless, this higher contrast exhibits the intrinic ability of this defect.

III. SUPPLEMENTARY NOTE 3

Magnetic-field, laser-power and microwave-power-dependent ODMR of Defect A.

Fig. S2 shows the ODMR spectra at seven magnetic fields between 30.4$\sim$36.1 mT at 100-μW laser power and 25-dBm microwave power, which exhibit the similar FWHM of the resonance.

Fig. S3 shows the ODMR spectra at different laser power and microwave power at 34-mT magnetic field. The FWHM of the resonance at different power suggests the power broadening phenomenon.

The corresponding FWHM values are shown in Fig. 5 of main text.

IV. SUPPLEMENTARY NOTE 4

Part of measurement results of the ultrabright color centers on the array sample. Table S1 shows nine ultrabright color centers whose emission rate exceeding 0.5 MHz under 100-μW laser excitation at 532

*These authors contributed equally to this work.
†Electronic address: lw691225@ustc.edu.cn
‡Electronic address: yitao@ustc.edu.cn
§Electronic address: tjs@ustc.edu.cn
¶Electronic address: gali.adam@wigner.hu
**Electronic address: cfli@ustc.edu.cn

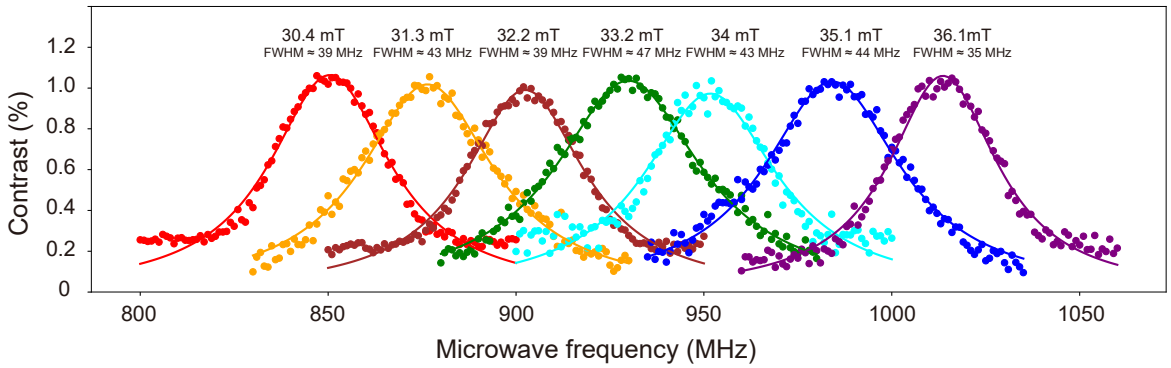

FIG. S2: **Magnetic-field-dependent ODMR of Defect A.** We measured the ODMR spectra at seven magnetic fields between 30.4∼36.1 mT at 100-μW laser power and 25-dBm microwave power. The ODMR spectra suggests the similar FWHMs of the resonance.

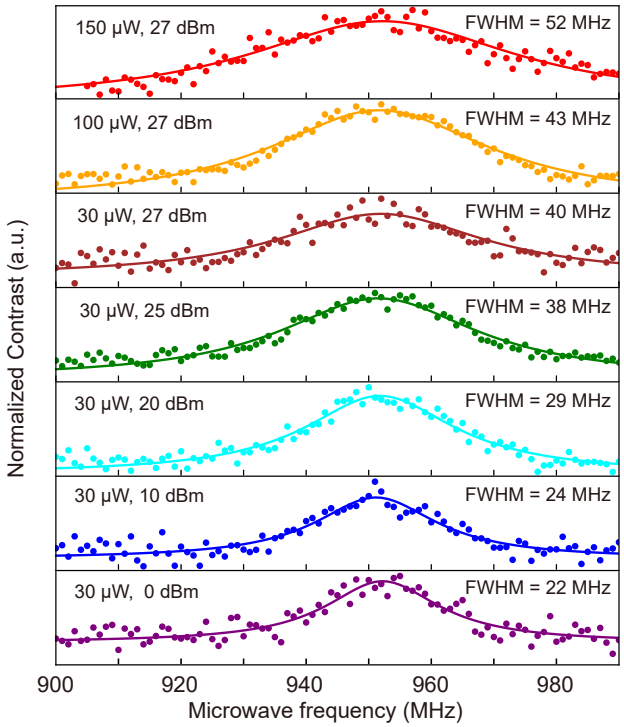

FIG. S3: **Laser-power and microwave-power-dependent ODMR of Defect A.** We measure the ODMR spectra at different laser power and microwave power at 34-mT magnetic field. The FWHM of the resonance at different power suggests the power broadening phenomenon.

nm, displaying a high probability to obtain the optically-detectable single spin among the bright spots in array. More importantly, these defects all exhibit the consistent optical properties (ZPL at 540±10 nm) and ODMR signals.

TABLE S1: List of part of the ultrabright color centers (>0.5 MHz) on the array sample under 100-μW laser excitation at 532 nm. Note: The spectra are truncated at 540 nm due to the 532-nm long-pass filter, and Defect F is bleached soon after laser excitation.

label	counts (10^5 /s)	ZPL (nm)	$g^{(2)}(0)$	ODMR
Defect A	7	546	0.25	√
Defect B	16	<540	0.37	√
Defect C	12	<540	0.63	√
Defect D	20	<540	0.62	√
Defect E	6	548	0.84	×
Defect F	6	–	0.64	–
Defect G	18	540	0.8	√
Defect H	11	<540	0.62	√
Defect I	14	<540	0.74	√

V. SUPPLEMENTARY NOTE 5

A type of previously-reported single spin defect. Except the new-found ultrabright single spin defect described here, we also find a type of single spin defect that has been reported before [1, 2], i.e., Defect J, as shown in Fig. S4(a). The photoluminescence count of Defect J is $\sim 1\times10^5$ counts/s under 100-μW laser excitation, which is lower than Defect A ($\sim 7\times10^5$ counts/s). Fig. S4(b) shows the room-temperature PL emission spectrum of Defect J, revealing ZPL at $\sim$ 576 nm and PSB at $\sim$ 588 nm. The second-order autocorrelation function $g^{(2)}(\tau)$ of Defect J is presented in Fig. S4(c),

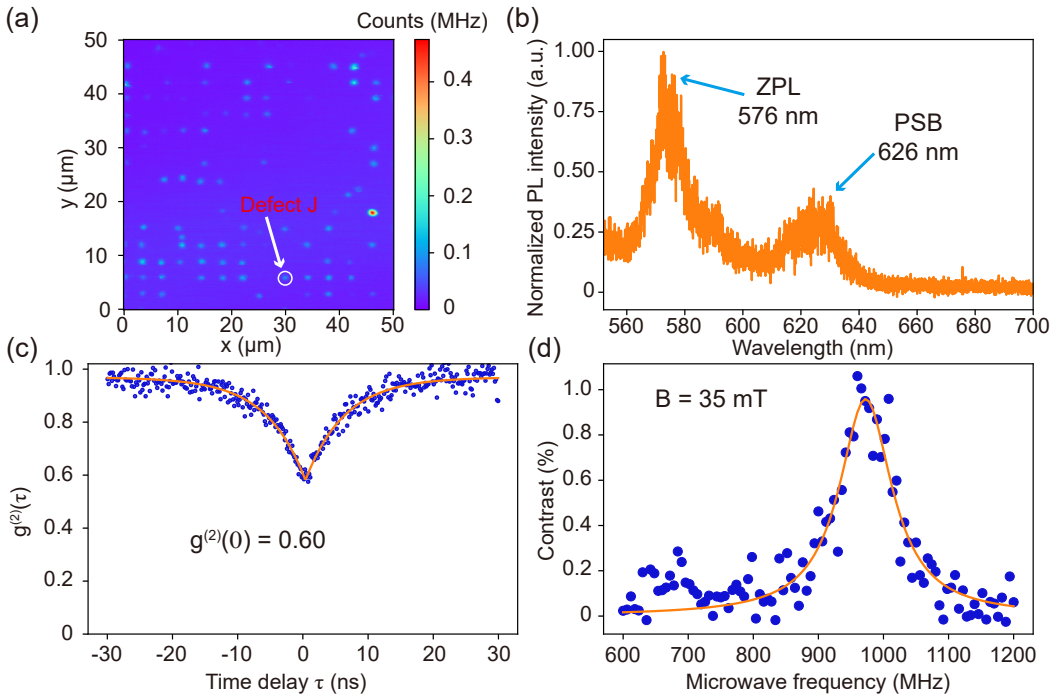

FIG. S4: **Optical and spin properties of Defect J.** (a) 50×50-μm^2 confocal PL map of hBN arrays with 100-μW laser excitation at 532 nm. Defect J is circled in the image. (b) Room-temperature photoluminescence spectrum of Defect J under 532-nm laser excitation. (c) Second-order autocorrelation measurement $g^{(2)}(\tau)$ of Defect J which is measured at 300-μW laser power. The blue dots are the experimental data, and the orange curve is a fit yielding $g^{(2)}(0) = 0.60$. (d) Room-temperature ODMR spectrum of Defect J at 300-μW laser power and 35-mT external magnetic field.

showing evidence of quantum emission but with background fluorescence contributions resulting in a $g^{(2)}(0)$ value of ~ 0.60. Fig. S4(d) displays the ODMR spectrum of Defect J at 35-mT external magnetic field, exhibiting a positive contrast of $\sim 1\%$ at 970 MHz. The optical and spin properties of defect J are consistent with carbon-related defects previously reported [1, 2], thus we can classify this type of defect as carbon-related defects. We want to note that Defect J actually does not reach the 0.5-MHz brightness shreshold, therefore, it is not in our list when we calculate the probabilities in Table II of main text.

VI. SUPPLEMENTARY NOTE 6

Other novel defects. Besides Defect A described in main text, we identify two different new defects which exhibit a measurable ODMR signal and are obviously distinct from Defect A, and they will be denoted to as Defect K and Defect L in the following. Figs. S5(a) and (d) display the photoluminescence spectra of Defect K and Defect L at room temperature. The spectra are truncated at 540 nm due to the limitation of our 532-nm long-pass filter. The ZPL of Defect K is below 540 nm. Defect L possesses a distinct ZPL at $\sim$ 546 nm and two relatively weak PSB at $\sim$ 565 nm and $\sim$ 588 nm. We also show in Figs. S5(b) and (e) that the second-order autocorrelation values at zero delay $g^{(2)}(0)$ for Defect K and Defect L are 0.53 and 0.39. Figs. S5(c) and (f) show the ODMR spectra of Defect K and L at room temperature. The ODMR spectrum of Defect K exhibits six hyperfine lines, and can be fitted well by a six-Lorentzian function. The results yield a hyperfine splitting constant $\sim$ 50 MHz, which is similar to the hyperfine structure of V_B^- defects [3]. Defect L possesses a positive high contrast of 7% and a relatively wide FWHM of 116 MHz.

VII. SUPPLEMENTARY NOTE 7

The defect level diagram of the positively charged C_BO_N at C_{2v} symmetry is shown in Fig. S6(a). There is an occupied b_2 state and empty b_2', a_2 states in the spin majority channel (spin-up channel in the figure). The wave function shows out-of-plane spatial distribution which is consistent with recent result about angular dependence analysis [4]. The transition dipole moment is oriented in plane. The hyperfine tensors are calculated for the nuclear spin active isotopes (^{13}C, ^{11}B and ^{14}N), as

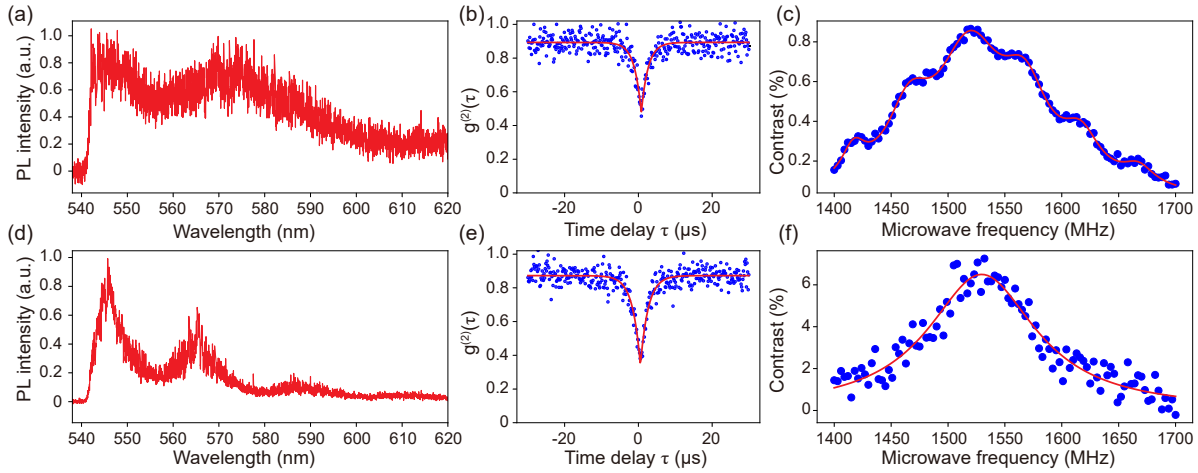

FIG. S5: **Optical and spin properties of Defect K and Defect L.** (a) Photoluminescence spectrum of Defect K. (b) Second-order autocorrelation measurement $g^{(2)}(\tau)$ of Defect K. (c) ODMR spectrum of Defect K. (d) Photoluminescence spectrum of Defect L. (e) Second-order autocorrelation measurement $g^{(2)}(\tau)$ of Defect L. (f) ODMR spectrum of Defect L. All measurements were performed with a 532-nm long-pass filter at 40-μW laser power and 54-mT magnetic field at room temperature.

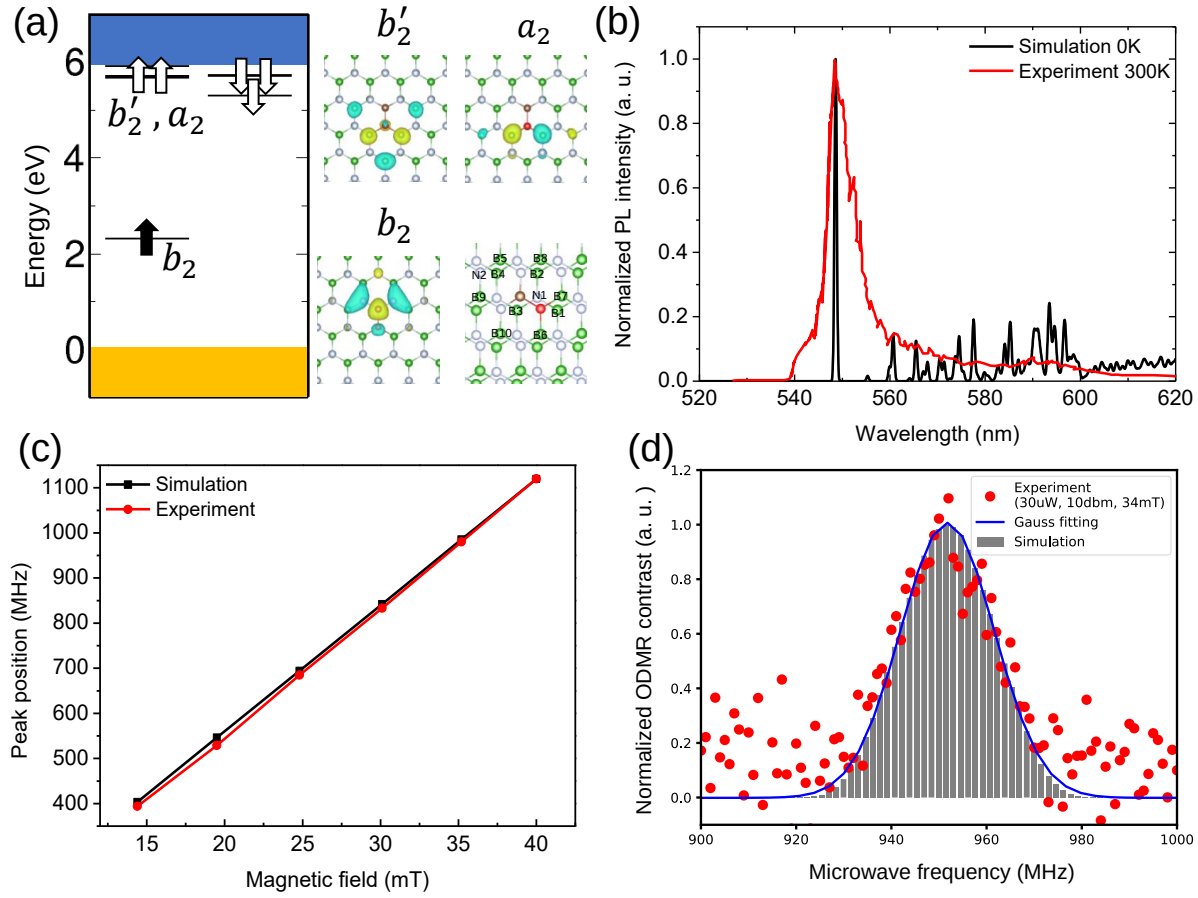

FIG. S6: **Simulated electronic and optical properties of C_BO_N.** (a) Kohn-Sham energy diagram of positive charge C_BO_N with the localized wavefunction. The labeled atoms are main contribution to hyperfine interaction. (b) Photoluminescence spectrum of C_BO_N at 0K (black line). (c) Dependence of ODMR resonance frequencies on the magnetic field. (d) Comparison between the simulated and experimental ODMR signals.

TABLE S2: The calculated hyperfine constants of the positively charged C_BO_N defect in MHz unit. The main contribution comes from the substituted carbon, first neighbor boron and nitrogen isotopes. The hyperfine constants are calculated for ^{11}B and ^{14}N.

atom	A_{xx}	A_{yy}	A_{zz}
^{13}C	23.94	24.12	271.48
^{11}B1	-0.94	-0.43	1.52
^{11}B2,3	-1.06	-0.55	1.78
^{11}B4	-0.44	0.13	1.36
^{11}B5,9	-2.44	0.25	2.33
^{11}B6,7	-1.55	-1.02	1.08
^{11}B8,10	-2.06	1.07	6.65
^{14}N1	-0.26	-0.23	1.05
^{14}N2	-0.50	-0.08	1.60
^{17}O	11.32	7.49	-13.53

TABLE S3: The calculated hyperfine constants of $C_B3O_NV_B$ defect in MHz unit. The main contribution comes from the substituted carbon, first neighbor boron and nitrogen isotopes. The hyperfine constants are calculated for ^{11}B and ^{14}N.

atom	A_{xx}	A_{yy}	A_{zz}
^{13}C	144.50	145.04	361.99
^{11}B	-0.66	2.02	7.02
^{11}B	-1.58	1.19	3.79
^{11}B	-1.60	1.01	3.28
^{11}B	-1.29	1.30	3.38
^{11}B	-2.67	0.89	2.88
^{14}N	-0.21	-0.16	7.10
^{14}N	-1.06	-0.84	5.51
^{17}O	-12.18	-10.03	-46.21

shown in Table S2. Although ^{13}C has active nuclear spin the natural abundance is low (1.1%) and, therefore, cannot contribute to the hyperfine splitting for about 99% of the single spin centers (similar to oxygen with less than 0.04% abundance). Due to the C_{2v} symmetry, the symmetrically equivalent atoms have the same hyperfine constants. ^{10}B (abundance 19.9%) might also occur for single spin centers in the experiment. Replacing ^{11}B with ^{10}B further decreases the linewidth.

The phonon side band (PSB) simulation is based on Franck-Condon approximation which can be described by the overlap between the phonon mode in ground and excited states. The maximum of the PSB is located at around 580 nm. The simulated PSB is larger than experimental result. However, the C_{2v} symmetry is Jahn-Teller unstable and the oxygen atom makes carbon atom move out-of-plane. This might due to the three bonding of oxygen. As a consequence, the calculated ZPL energies will be lower and the Debye-Waller factor will be higher in the low-symmetry configuration with respect to the C_{2v} configuration, and the calculated hyperfine constants are also affected considerably in the electronic ground state.

We consider the positively charged double C_B ($2C_B$) and triple neutral C_B ($3C_B$) and find the ZPLs are smaller than observed one [9, 10]. The ODMR spectra are quite similar to that of the single C_B defect with linewidth of around 50 MHz. Increasing the C_B-C_B distance in $2C_B$ decreases the energy difference between two defect orbitals and decreases the ZPL energy. C_2C_B has ODMR width about 27 MHz but the ZPL is out of the observed range [7]. Recently C_2C_N is considered as a possible single photon emitter with ZPL at 2.33 eV for the second optical transition [8]. The simulated ODMR linewidth is 51 MHz. This might be related to the defect L in our study considering the power broadening. Here, we cannot exclude the possibility of C_N due to the same reason. Unfortunately, this effect cannot be simulated currently. Beside the carbon related defects, other configurations are also calculated. For intrinsic defects, the negatively charged boron antisite (B_N) has a ZPL at around 2.324 eV with $S = 1.83$, however, the FWHM of the ODMR broadening is 153 MHz. The positively charged nitrogen antisite (N_B) has a ZPL energy at 2.920 eV which is out of the ballpark of the observed ZPL energies of single photon emitters in our study.

The gyromagnetic ratios are large both for boron and nitrogen isotopes, and their interaction with the electron spin generates a broad ODMR signal. The relatively narrow ODMR linewidth in experiment is related to the spin density localization on either nuclear spin free isotopes with high natural abundance or nuclear spin isotopes with small gyromagnetic ratio, and then the spin density overlaps with neighbor boron and nitrogen atoms with non-zero nuclear spins. The likely impurity candidates are carbon, oxygen and silicon atoms. Oxygen on boron site (O_B) has extremely high formation energy as indicated before, and oxygen on nitrogen site (O_N) only has one occupied state close to CBM which cannot be responsible for the observed transition [5]. Neither silicon substitution is a good candidate since its optical excitation energy is around 4 eV [6], and it is not a common defect without intentional doping. Donor-acceptor pairs

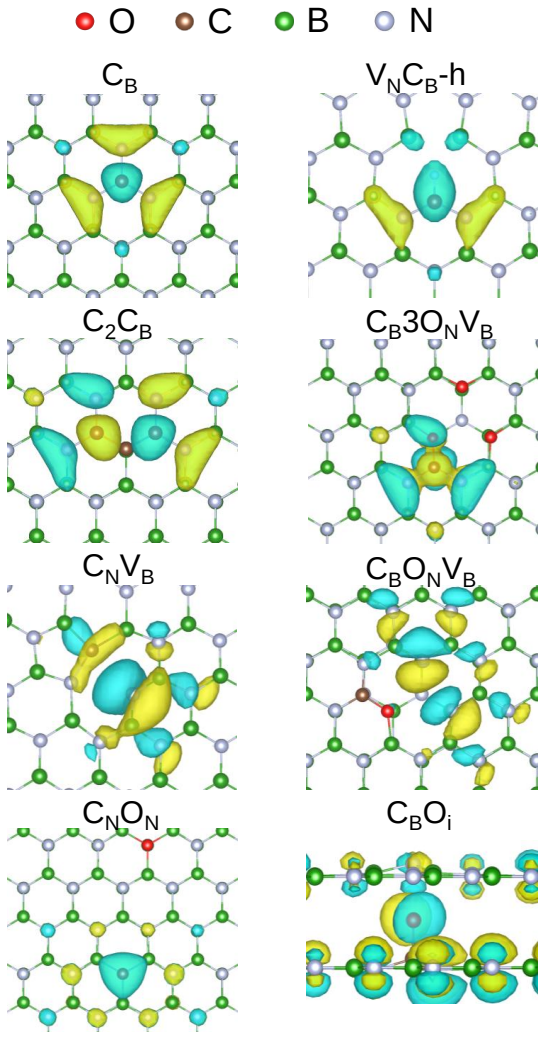

FIG. S7: **Single spin wavefunction of proposed defects.** Pure carbon related defects can be found in Refs. [7, 8, 10].

(DAPs) are also good candidates for the quantum emitters. DAPs with native defects included (C_BB_N, C_NN_B, C_BN_B, C_NB_N, B_NO_N, N_BO_N) have large coupling on native antisite defects. With positively charged, C_BO_N and C_NO_N can have ZPL around 2.3 eV depending on the distance between the pairs. The shortest distance C_BO_N pair has an ODMR linewidth of 23 MHz in the positive charge state. We find that the positively charged C_NO_N-$\sqrt{7}a$ (a is the lattice constant of hBN) has an ODMR linewidth of 119 MHz, and the optical signal comes at ZPL of 2.30 eV with $S = 2.38$ HR factor. We conclude that this defect can also be a reasonable candidate for defect L. Further detailed investigation on DAPs might reveal the nature of the single spin species in hBN but we here focus on the most characterized defect A in our study. In Figure S7, we plot the singly occupied Kohn-Sham wavefunction of several defects we consider here that is mostly associated with the spin density distribution. C_B is the defect we studied before and the major contribution of hyperfine interaction comes from neighboring nitrogen atoms. Consequently, we speculate the narrow linewidth is due to the substitution of nitrogen with nuclear spin inactive elements discussed above. Removing one nitrogen creates V_NC_B structure which is a singlet. We then use hydrogen to passivate the carbon dangling bond. This is a doublet spin system, however, the hydrogen has large hyperfine contribution. Thus hydrogen is unlikely to exist in the defect A. The in-plane dangling bonds form in-plane distribution wavefunction and it ultimately leads to interaction with the nuclear spins from boron and nitrogen, for example in the negatively charged V_NC_B and $C_BO_NV_B$ defects. Therefore, the in-plane dangling bonds should be avoided which also means that the $sp2$ bonding type should be well preserved. Another example is C_BO_i where oxygen is an interlayer interstitial impurity. Carbon atom is pulled out of plane and transforms to $sp3$ bonding type which distributes wavefunction on the nearby nitrogen atoms. The ODMR spectra of C_NO_N-$\sqrt{7}a$ is very similar to C_N because the long distance between oxygen and carbon impurity atoms. The oxygen atom should be placed near carbon atom to reduce hyperfine interaction from boron or nitrogen (C_BO_N and $C_B3O_NV_B$). The calculated hyperfine constants of these defects are listed in Tables S2 and S3. Indeed, the hyperfine constants on the immediate two nitrogen neighbors is moderate with producing relatively narrow FWHM in the ODMR spectrum. On the other hand, the calculated optical properties are not fully consistent with the high Debye-Waller factor and the ZPL energy at about 2.28 eV. Therefore, we concluded that these type of defects could be the core structures of more extended defects to where the spin density is localized but its optical properties are perturbed by the presence of other nearby defects.

[1] Mendelson, N. *et al.* Identifying carbon as the source of visible single-photon emission from hexagonal boron nitride. *Nature Mater.* **20**, 321-328 (2021).

[2] Stern, H. L. *et al.* Room-temperature optically detected magnetic resonance of single defects in hexagonal boron nitride. *Nat. commun.* **13**, 618 (2022).

[3] Gottscholl, A. *et al.* Initialization and read-out of intrinsic spin defects in a van der Waals crystal at room temperature. *Nature Mater.* **19**, 540-545 (2020).

[4] Chejanovsky, N. *et al.* Single-spin resonance in a van der Waals embedded paramagnetic defect. *Nat. Mater.* **20**, 1079-1084 (2021).

[5] Weston, L., Wickramaratne, D., Mackoit, M., Alkauskas, A. & Walle, C. Native point defects and impurities in hexagonal boron nitride. *Phys. Rev. B* **97**, 214104 (2018).

[6] Smart, T., Li, K., Xu, J. & Ping, Y. Intersystem crossing and exciton-defect coupling of spin defects in hexagonal boron nitride. *NPJ Comput. Mater.* **7**, 1-8 (2021).

[7] Auburger, P., & Gali, A. Towards ab initio identification of paramagnetic substitutional carbon defects in hexagonal boron nitride acting as quantum bits. *Phys. Rev. B* **104**, 075410 (2021).

[8] Li, K., Smart, T. & Ping, Y. Carbon trimer as a 2 eV single-photon emitter candidate in hexagonal boron nitride: A first-principles study. *Phys. Rev. Mater.* **6**, L042201 (2022).

[9] Wang, D., Ciccarino, C., Flick, J. & Narang, P. Hybridized defects in solid-state materials as artificial molecules. *ACS Nano* **15**, 5240-5248 (2021).

[10] Li, S., Pershin, A., Thiering, G., Udvarhelyi, P. & Gali, A. Ultraviolet Quantum Emitters in Hexagonal Boron Nitride from Carbon Clusters. *J. Phys. Chem. Lett.* **13**, 3150-3157 (2022).